Supplemental Material: Structural symmetry effects on the competition of density waves and superconductivity in bilayer nickelates

Steffen Bötzel,[1,*] Aiman Al-Eryani,[1,*] Jun Zhan,[2,3] Xianxin Wu,[4]
Frank Lechermann,[1] Michael M. Scherer,[1] and Ilya M. Eremin[1]

[1] *Theoretische Physik III, Fakultät für Physik und Astronomie, Ruhr-Universität Bochum, D-44780 Bochum, Germany*
[2] *Beijing National Laboratory for Condensed Matter Physics and Institute of Physics, Chinese Academy of Sciences, Beijing 100190, China*
[3] *School of Physical Sciences, University of Chinese Academy of Sciences, Beijing 100190, China*
[4] *Institute for Theoretical Physics, Chinese Academy of Sciences, Beijing, China*

Computational details and details on the superconducting instability

We used a 100×100 momentum grid for the fRG flows at ambient pressure and a 141×141 momentum grid for the high-pressure phase. The grids effectively result in the same momentum resolution because the folded Brillouin Zone is a factor of 2 smaller. To evaluate the bubbles, an additional refinement factor of 4 is used for the momentum grids. For the presented data only intra unit cell bonds are used allowing better momentum resolution. However, we checked the role of higher order bonds to nearest and second nearest neighbors. The real space gaps for bonds to nearest neighbors are negligible. The gaps for the second nearest neighbors were found to be partially finite but without any qualitative impact on any of the presented results. The gap amplitudes are in agreement with a previous fRG study [S1].

The relative gap amplitudes for the superconducting instabilities are listed exemplarily for the high-pressure phase in table I. The values for ambient pressure scenarios are very similar. The interlayer d_{z^2} term is always the dominant component with the dominance being largest for $\delta\epsilon^-$. This is expected because the odd susceptibility is most dominant for that case.

J (eV)	$\delta\epsilon = \delta\epsilon^+$	$\delta\epsilon^*$	$\delta\epsilon^-$
0.2	-	$\begin{pmatrix} -0.448 & 0.100 \\ 0.537 & -0.014 \end{pmatrix}$	-
0.4	$\begin{pmatrix} -0.449 & 0.120 \\ 0.524 & 0.095 \end{pmatrix}$	$\begin{pmatrix} -0.394 & 0.094 \\ 0.577 & 0.055 \end{pmatrix}$	$\begin{pmatrix} -0.109 & 0.115 \\ 0.676 & 0.132 \end{pmatrix}$
0.5	$\begin{pmatrix} -0.437 & 0.110 \\ 0.534 & 0.112 \end{pmatrix}$	$\begin{pmatrix} -0.380 & 0.088 \\ 0.585 & 0.074 \end{pmatrix}$	$\begin{pmatrix} -0.193 & 0.010 \\ 0.659 & 0.135 \end{pmatrix}$
0.6	-	$\begin{pmatrix} -0.368 & 0.083 \\ 0.519 & 0.088 \end{pmatrix}$	-

TABLE I. **Relative real-space gap amplitudes for the superconducting instability for different J.** Results are shown for the high-pressure phase in the format $\begin{pmatrix} \Delta^z_\parallel & \Delta^x_\parallel \\ \Delta^z_\perp & \Delta^x_\perp \end{pmatrix}$, where $\Delta_\parallel$ denotes the on-site component. The square sum of all gap components is normalized to one.

Details on the role of Hund's coupling and comparison of μ and $\delta\epsilon$ variations

In Fig. S1, the critical flow parameters for the different instabilities are shown as a function of $\delta\epsilon$ and the chemical potential μ for the ambient-pressure phase in both the low-J and high-J regimes. In the low-J regime, the critical scale exhibits a maximum in the vicinity of $\delta\epsilon^*$ for both the $\delta\epsilon$ and μ variations. Once the γ pocket is shifted below the Fermi level, the instability is rapidly suppressed, whereas increasing $\delta\epsilon$ beyond $\delta\epsilon^*$ leads to a more gradual suppression.

In contrast, the high-J regime shows only a weak dependence on $\delta\epsilon$. In particular, no maximum is observed near $\delta\epsilon^*$ when varying $\delta\epsilon$. However, when varying μ, the leading instability changes rapidly to the SDW state once the γ pocket falls below the Fermi level. The high-pressure phase exhibits qualitatively the same behavior (not shown).

The different behavior observed for the $\delta\epsilon$ and μ variations can be traced back to the distinct evolution of the α and β Fermi surface sheets. The corresponding Fermi surfaces are shown in Fig. S2. Starting from the reference case in which the γ band touches the Fermi level, $\delta\epsilon$ and μ are varied such that the top of the γ band lies either 50 meV above or 50 meV below the Fermi level. Importantly, for the case in which the γ band is shifted 50 meV above the Fermi level, the α and β sheets evolve in opposite directions depending on whether the change is induced by varying $\delta\epsilon$ or μ. Once the γ band is below the Fermi level, increasing $\delta\epsilon$ has little impact on the size of α and β Fermi surface sheets.

The low and high J behavior can be understood by considering the magnetic susceptibilities shown in Fig. S3. In the low-J regime, the system is further away from the critical interaction strength J_c. For both $\delta\epsilon^*$ and $\delta\epsilon^+$, the susceptibility exhibits significant contributions not only near $\mathbf{Q}$ and $\tilde{\mathbf{Q}}$ but also around $(\pi, 0)$ and $(0, \pi)$. These contributions appear to cooperate in promoting the superconducting instability. Once the latter contributions disappear as the γ pocket drops below the Fermi level, the superconducting instability is likewise strongly suppressed.

At higher J, the susceptibility is dominated by pronounced contributions near $\mathbf{Q}$ and $\tilde{\mathbf{Q}}$, while the weight around $(\pi, 0)$ and $(0, \pi)$ is also substantial. These dominant magnetic fluctuations largely determine the instability, rendering the additional contributions associated with the γ pocket comparatively unimportant.

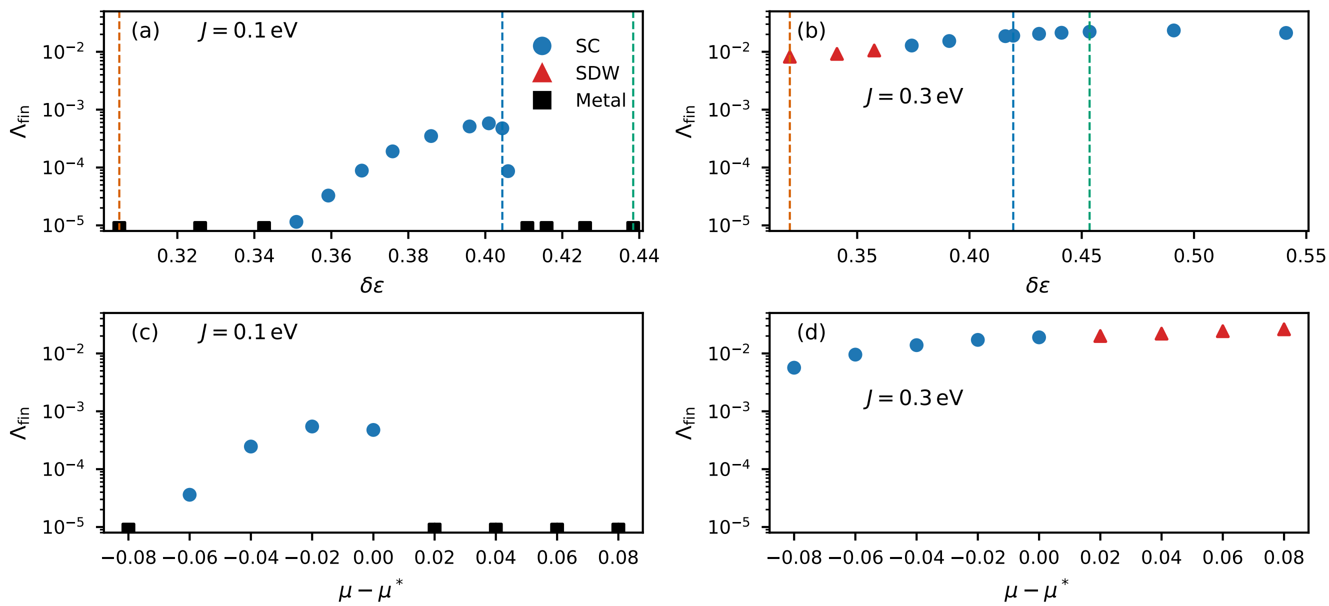

FIG. S1. **Scan of leading instabilities within fRG for the ambient-pressure phase for $\delta\epsilon$ and chemical potential μ variation**. (**a**,**b**) Variation of $\delta\epsilon$ at low $J = 0.1$ eV and high $J = 0.3$ eV, respectively. Dashed lines denote $\delta\epsilon^+$, $\delta\epsilon^*$ and $\delta\epsilon^-$ values. (**c**,**d**) Variation of μ with respect to the chemical potential μ^* for the $\delta\epsilon^*$ case, respectively. The corresponding fillings for the chemical potential scan are $n = 3 + \delta$ with δ reaching from $\delta = -0.14$ to $\delta = 0.05$.

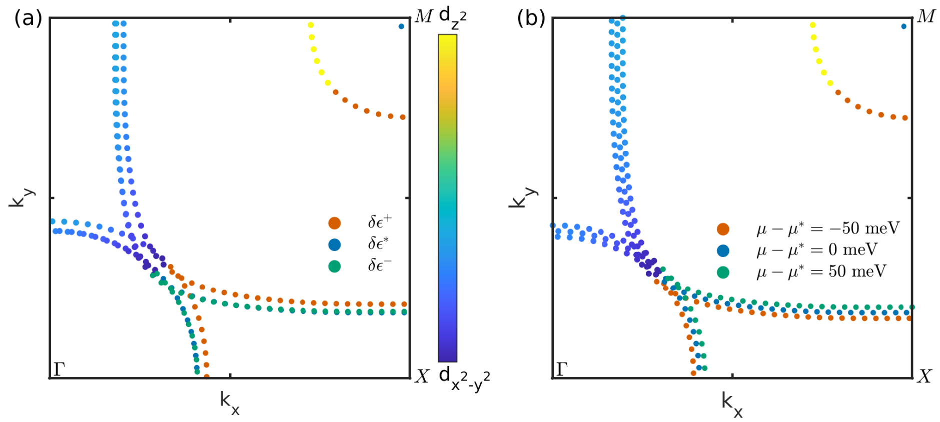

FIG. S2. **High-pressure Fermi surface variations with $\delta\epsilon$ and chemical potential $\mu - \mu^*$** (**a**) Variation of $\delta\epsilon$. The $\delta\epsilon^*$ points are mostly hidden behind $\delta\epsilon^-$ points. (**b**). Variation of $\mu - \mu^*$, where μ^* denotes the reference chemical potential for the $\delta\epsilon^*$ case and half-filling. The fillings for $\mu = \pm 50$ meV are $n = 3 + \delta$ with $\delta = 0.03$ and $\delta = -0.09$.

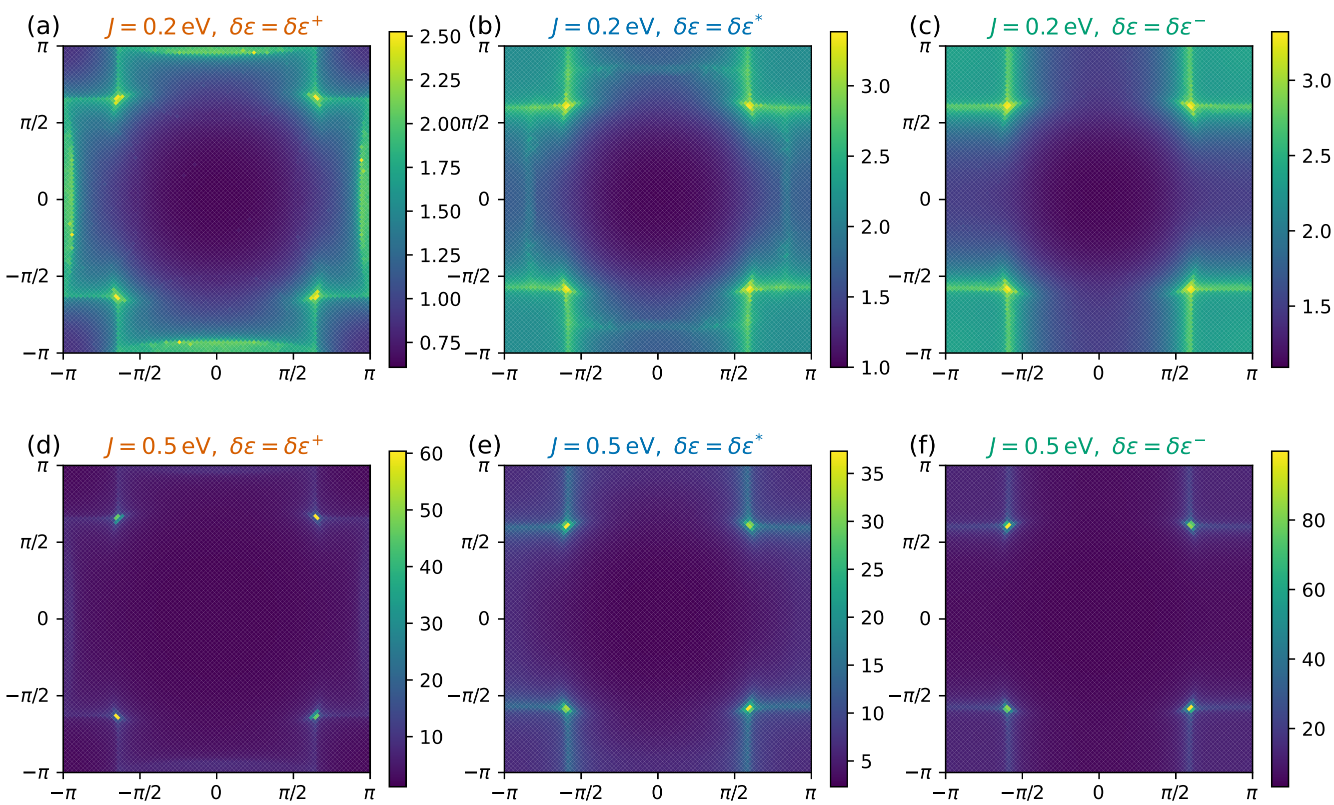

FIG. S3. **Odd magnetic susceptibilities in the high-pressure phase at the critical flow parameters in the high and low J regimes for different locations of the γ band.** (**a**,**b**,**c**) Low J regime with $J = 0.2$ eV for $\delta\epsilon = \delta\epsilon^+$, $\delta\epsilon^*$ and $\delta\epsilon^-$, respectively. (**d**,**e**,**f**) Corresponding results for the high J regime with $J = 0.5$ eV. Only in the low J regime and when the γ band crosses the Fermi level, additional peaks at $(\pi, 0)$ and $(0, \pi)$ ($\mathbf{Q}_2$) contribute significantly.

Band structure and bare susceptibilities for ambient pressure with uniaxial strain

The band structure for the ambient-pressure model (Fig. S4(b)) with strain is compared to the ambient-pressure model (Fig. S4(a)). The strain enlarges the bandwidth from 3.35 eV to 3.92 eV for $\delta\epsilon = \delta\epsilon^*$ (the high-pressure bandwidth is 4.11 eV). The Fermi surface for the uniaxial strain model (Fig. S4(d)) is almost C_4 symmetric.

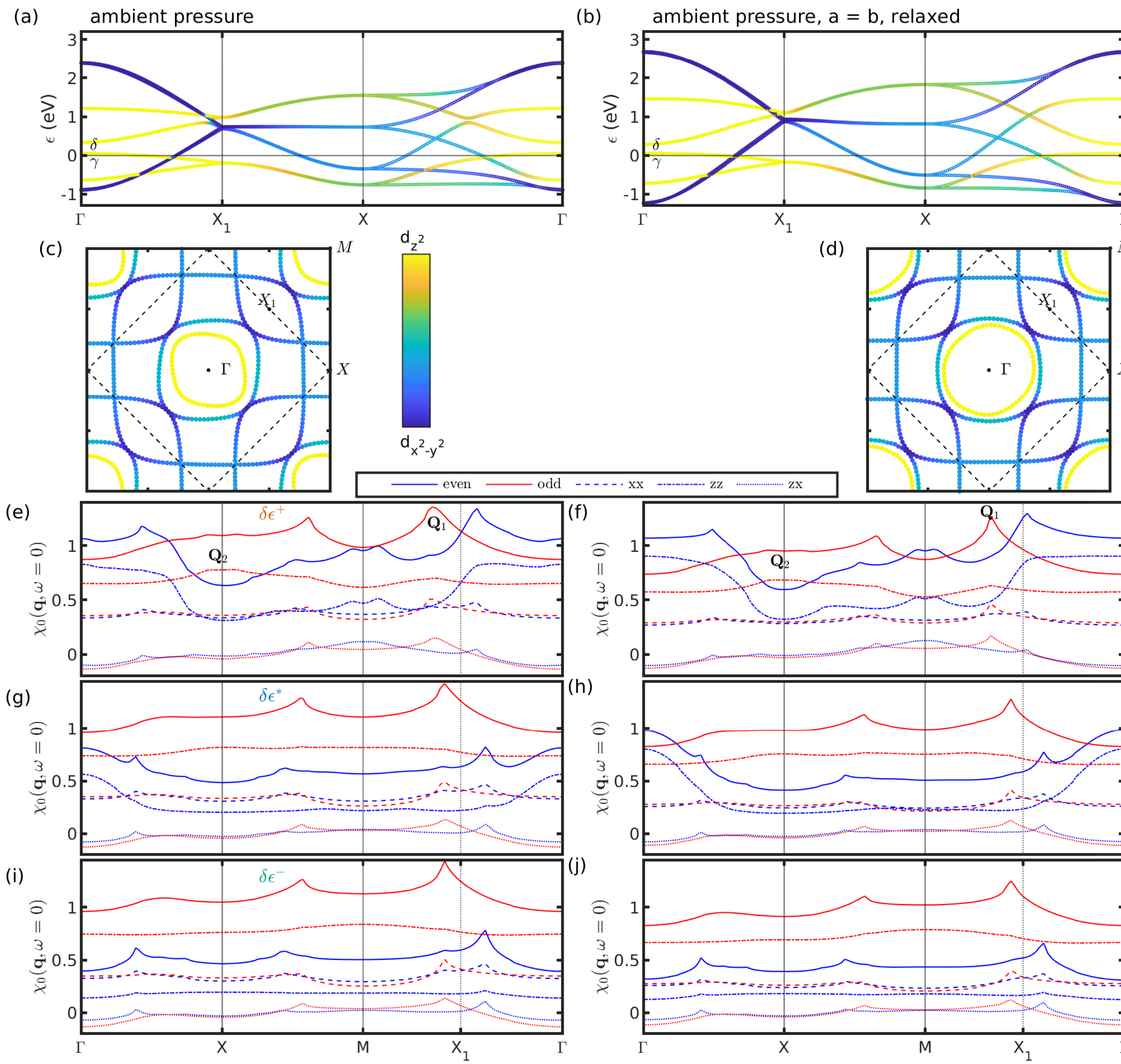

FIG. S4. **Band structure, Fermi surface and non-interacting susceptibility of $La_3Ni_2O_7$ at ambient pressure with modeled strain.** (**a**,**b**) Band structure for the ambient-pressure model along *Amam* high symmetry path for $\delta\epsilon = \delta\epsilon^*$ without strain and with strain, respectively. (**c**,**d**) Fermi surfaces corresponding to the two cases for $\delta\epsilon = \delta\epsilon^+$. (**e**)-(**j**) Total and orbital resolved contributions to the non-interacting susceptibilities for the top of the γ band for $\delta\epsilon^+$, $\delta\epsilon^*$ and $\delta\epsilon^-$ for the three cases. The ambient-pressure data for the case without strain is the same as in Fig. **??** and repeated here for an easier comparison.

SUPPLEMENTARY REFERENCES

* These authors contributed equally to this work.
[S1] J. Zhan, C. Le, X. Wu, and J. Hu, Impact of nonlocal coulomb repulsion on superconductivity and density-wave orders in bilayer nickelates, npj Quantum Materials (2026).